nature nanotechnology

Article

https://doi.org/10.1038/s41565-023-01558-1

Spontaneous broken-symmetry insulator and metals in tetralayer rhombohedral graphene

Received: 21 June 2023

Accepted: 30 October 2023

Published online: 23 November 2023

Check for updates

Kai Liu[1,6], Jian Zheng[1,6], Yating Sha[1], Bosai Lyu[1], Fengping Li[2], Youngju Park[2], Yulu Ren[1], Kenji Watanabe[3], Takashi Taniguchi[4], Jinfeng Jia[1], Weidong Luo[1], Zhiwen Shi[1], Jeil Jung[2,5] ✉ & Guorui Chen[1] ✉

Interactions among charge carriers in graphene can lead to the spontaneous breaking of multiple degeneracies. When increasing the number of graphene layers following rhombohedral stacking, the dominant role of Coulomb interactions becomes pronounced due to the significant reduction in kinetic energy. In this study, we employ phonon–polariton-assisted near-field infrared imaging to determine the stacking orders of tetralayer graphene devices. Through quantum transport measurements, we observe a range of spontaneous broken-symmetry states and their transitions, which can be finely tuned by carrier density n and electric displacement field D. Specifically, we observe a layer-antiferromagnetic insulator at $n = D = 0$ with a gap of approximately 15 meV. Increasing D allows for a continuous phase transition from a layer-antiferromagnetic insulator to a layer-polarized insulator. By simultaneously tuning n and D, we observe isospin-polarized metals, including spin–valley-polarized and spin-polarized metals. These transitions are associated with changes in the Fermi surface topology and are consistent with the Stoner criteria. Our findings highlight the efficient fabrication of specially stacked multilayer graphene devices and demonstrate that crystalline multilayer graphene is an ideal platform for investigating a wide range of broken symmetries driven by Coulomb interactions.

When the Coulomb interaction dominates over kinetic energy, the degeneracies of spin and valleys in graphene can be lifted, and the competition among energies of different degrees of freedom can lead to rich broken-symmetry phases[1–5]. For monolayer graphene, however, linear energy dispersion hinders spontaneous broken symmetries due to the large kinetic energy (Fig. 1a). Although the application of a strong magnetic field or the twisting of graphene layers can reduce the kinetic energy[6–10], studying the physics of Landau levels or moiré flat bands necessitates the consideration of additional complex energy factors or the involvement of large unit cells, respectively. These complexities

[1]Key Laboratory of Artificial Structures and Quantum Control (Ministry of Education), Shenyang National Laboratory for Materials Science, School of Physics and Astronomy, Shanghai Jiao Tong University, Shanghai, China. [2]Department of Physics, University of Seoul, Seoul, Korea. [3]Research Center for Electronic and Optical Materials, National Institute for Materials Science, Tsukuba, Japan. [4]Research Center for Materials Nanoarchitectonics, National Institute for Materials Science, Tsukuba, Japan. [5]Department of Smart Cities, University of Seoul, Seoul, Korea. [6]These authors contributed equally: Kai Liu, Jian Zheng. ✉e-mail: jeiljung@uos.ac.kr; chenguorui@sjtu.edu.cn

https://doi.org/10.1038/s41565-023-01558-1

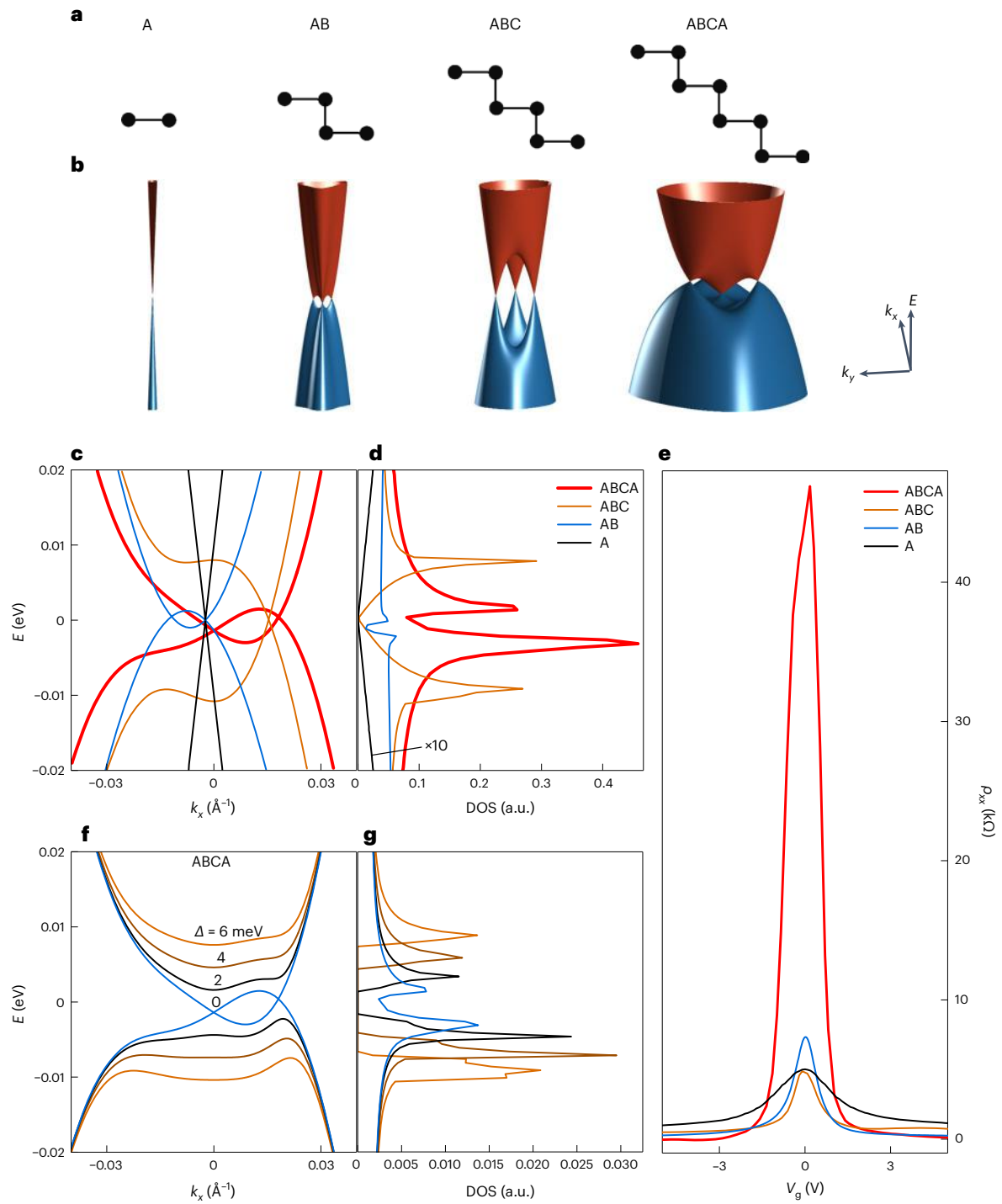

Fig. 1 | Rhombohedral graphene family. a,**b**, Unit cells (**a**) and band structures (**b**) of monolayer, AB bilayer, ABC trilayer and ABCA-4LG. The conduction and valence bands are shown in red and blue, respectively. **c**,**d**, Linecuts of band structures along the k_x direction when $k_y = 0$ (**c**) and DOS versus energy from monolayer to tetralayer (**d**). The value of the DOS of monolayer graphene is amplified by a factor of 10 in **d** for visibility. **e**, Experimentally measured gate-dependent resistivity of different graphene layers in similar sample qualities. Data were obtained at $T = 1.5$ K. **f**,**g**, Band structures (**f**) and DOS (**g**) of ABCA-4LG with the applied interlayer energy differences.

go beyond the scope of the simple intrinsic graphene model. In this regard, an alternative and more straightforward approach to enhance Coulomb interactions is by increasing the number of layers through rhombohedral stacking[11–15].

Rhombohedral graphene, characterized by an ABCABC… stacking sequence, exhibits a dispersion relation $E_k \approx p^N$, where E_k is the kinetic energy, p is the momentum and N is the number of layers[16–18]. Consequently, the kinetic energy can be significantly reduced in thicker graphene. Figure 1a,b illustrates the unit cell and the calculated band structures at the K point of rhombohedral graphene, ranging from monolayer to ABCA tetralayer graphene (ABCA-4LG). The presence of interlayer hopping results in pronounced trigonal warping and enhanced Van Hove singularities (VHS) near the charge-neutrality point (CNP) as N increases, as demonstrated by the linecut and density of

states (DOS) (Fig. 1c,d). Considering the strong Coulomb interactions, the substantial DOS at CNP and VHS can lead to instabilities of the Fermi circles, potentially giving rise to new ground states with broken symmetries. The band structure and correlations of rhombohedral graphene can be significantly tuned by a vertical electric displacement field D, which contributes to the energy difference Δ between the top and bottom layers (Fig. 1f,g). Specifically, ABCA-4LG can open a gap at CNP along with a modification in its correlation, layer polarization and VHS.

Based on the calculated DOS derived from single-particle band structures, we initially anticipated that ABCA-4LG would exhibit lower resistivity (higher conductivity) compared with thinner layers due to its larger DOS. However, our experimental findings (Fig. 1e) demonstrate a significantly higher resistivity for ABCA-4LG compared with monolayer (A), bilayer (AB) and trilayer (ABC) graphene at CNP ($V_g = 0$), when the temperature is $T = 1.5$ K. It is important to note that all the graphene layers presented in Fig. 1e are on a hexagonal boron nitride (hBN) substrate, which mitigates qualitative differences in electron–hole puddles, charge mobility and dielectric screening effects. Consequently, the observed giant resistivity peak in ABCA-4LG is deemed to be intrinsic in nature.

Phonon–polariton-assisted near-field imaging

To systematically study the unexpected resistivity peak of ABCA-4LG, the high-quality dual-gated device is necessary, as it enables the independent tuning of n and D. Earlier experiments of moiré-less ABCA-4LG systems had been carried out for suspended samples with limited accessible electron densities and electric fields[13] or with scanning probe microscopes for the larger ABCA domains in marginally twisted double bilayer graphene[19]. The fabrication of high-quality rhombohedral graphene devices thicker than a bilayer poses a challenge. Although rhombohedral stacking naturally exists as domains in bulk graphite and exfoliated thin layers, it is energetically metastable and easy to transition into Bernal stacking during the fabrication process such as dry transfer. Therefore, it is crucial to effectively monitor the stacking orders throughout the fabrication process, particularly after hBN coverage, as traditional tools like Raman spectroscopy are not readily applicable in these cases.

To address this challenge, we employed a phonon–polariton-assisted near-field optical imaging technique, which enabled the identification of rhombohedral and Bernal graphene across the hBN flake coverage. Such penetration imaging was conducted on a scanning near-field optical microscopy (SNOM) system (Extended Data Fig. 1a), known for its capability to image the stacking orders of on-surface graphene[20,21]. However, when graphene is covered by an hBN flake, conventional near-field optical imaging of graphene becomes inaccessible due to the highly localized near field and strong screening effect of the hBN flake. To image the embedded graphene, we carefully selected a specific excitation frequency that lies in one of the Reststrahlen bands of hBN (Fig. 2a). At this frequency, hBN behaves as a waveguide[22,23], transmitting the optical response of the graphene located beneath the hBN slab to its top surface (Fig. 2b and Methods).

In our experimental approach, after identifying the number of exfoliated graphene layers by optical contrast and SNOM, we used the in situ atomic force microscopy (AFM) cutting technique[24] to isolate the ABCA domains from ABAB stacks. Subsequently, these domains were encapsulated by hBN thin films. Following the encapsulation, both ABCA and ABAB graphene domains become invisible in terms of topography and near-field optical imaging (Fig. 2c,d). To visualize the ABCA and ABAB domains, we finely adjusted the excitation frequency to match one of the Reststrahlen bands of hBN. This allowed the ABCA and ABAB domains to become distinguishable (Extended Data Fig. 1b–m), with the maximum contrast observed at 1,550 cm^{-1} (Fig. 2e). By using the phonon–polariton-assisted near-field optical imaging technique, we successfully fabricated a few moiré-less hBN/ABCA-4LG/hBN devices with dual gates. A schematic of a typical device's side view and an optical image are presented in Fig. 2f,g, respectively. The implementation of the top and bottom gates provides independent control over n and D of ABCA-4LG (Methods).

Broken-symmetry insulators at $n = 0$

Through quantum transport measurements, we have observed two distinct insulating phases at $D = 0$ and $D \neq 0$ at CNP ($n = 0$) (Fig. 3a). The colour plot represents the measured resistivity ρ_{xx} as a function of n and D at $T = 1.5$ K. The insulating nature of these two phases is further confirmed by the temperature-dependent resistivity curves shown in Fig. 3b, which presents the linecut along D at $n = 0$ for varied temperatures. From the Arrhenius plot of the temperature dependence of ρ_{xx} (Extended Data Fig. 2), we can estimate a transport gap Δ of the insulator at $n = D = 0$ to be approximately 15 meV. As shown in Extended Data Fig. 3, the resistivity peak at $D = 0$ flattens out at high temperatures, suggesting a phase transition of spontaneous symmetry breaking. Furthermore, we observe that this gap linearly decreases with D and eventually vanishes at $|D| \approx 0.1$ V nm^{-1} (Fig. 3c). In the case of the insulator at $D \neq 0$, the gap emerges when $|D| > 0.15$ V nm^{-1} and linearly increases with $|D|$. These two insulating phases are connected by a low-resistivity region spanning $|D| \approx 0.10$–0.15 V nm^{-1}. In particular, this low-resistivity state exhibits a metallic behaviour at low temperatures when $T < 14$ K (Extended Data Fig. 2e).

Similar to AB bilayer[11,25–27] and ABC trilayer graphene[12,28], the insulating state observed at large $|D|$ in ABCA-4LG can be attributed to a layer-polarized insulator (LPI) resulting from the broken inversion symmetry. The low-energy conduction and valence bands of ABCA-4LG arise from the orbitals of the two diagonal sublattices in the top and bottom layers, where a positive D in LPI induces a negative mass term between those two sublattices regardless of the spin–valley flavours. When a large D is applied (Fig. 3c, inset), the inversion symmetry of the top and bottom sublattices is broken; the valence and conduction bands are contributed from different layers, leading to the opening of an LPI gap whose size is linearly dependent on D.

In contrast to the AB bilayer and ABC trilayer cases, the insulating state observed at $D = 0$ in ABCA-4LG is unexpected based on the single-particle band structures, which predict the presence of finite DOS at zero energy. The dashed line in Fig. 3c represents the calculated single-particle gap at different D values. Interestingly, the observed unexpected gap nearly emerges when the calculated gap is zero, indicating the existence of finite carriers arising from the overlap between valence and conduction bands in the single-particle picture. We argue that the insulating state observed at $n = D = 0$ originates from a layer-antiferromagnet (LAF) (Fig. 3c, middle inset) state of the finite carriers in ABCA-4LG, where the opposite Dirac mass terms for opposite spins induce a spin-layer polarization.

Theoretical predictions have identified all the possible insulating ground states with different broken symmetries in rhombohedral graphene. The layer pseudospin polarization, namely, the layer-resolved charge distribution of the four spin–valley flavours, can be classified as flavour antiferromagnetic (AF) for the layer-charge-balanced configuration, the flavour ferrimagnetic (Fi) for partial layer-charge polarization and flavour ferromagnetic (F) for full layer-charge polarization[1,29]. These phases often have associated quantum Hall phases due to the Berry curvatures at the Dirac points and they include the quantum anomalous Hall, LAF and quantum spin Hall effects for the layer-charge-balanced flavour AF phase; the quantum valley Hall effect for the flavour F phase; and ALL state with partial layer-charge polarization for the flavour Fi phase[4,29] (Extended Data Figs. 5 and 6 provide more specific definitions of these states). However, we can first rule out the quantum anomalous Hall, quantum spin Hall and ALL states as they would exhibit quantized longitudinal and Hall resistivities, which are absent in our measurements. Additionally, the quantum valley Hall effect can be ruled out since it requires a charge-layer polarization, which corresponds to a non-zero D. Therefore, the only remaining

https://doi.org/10.1038/s41565-023-01558-1

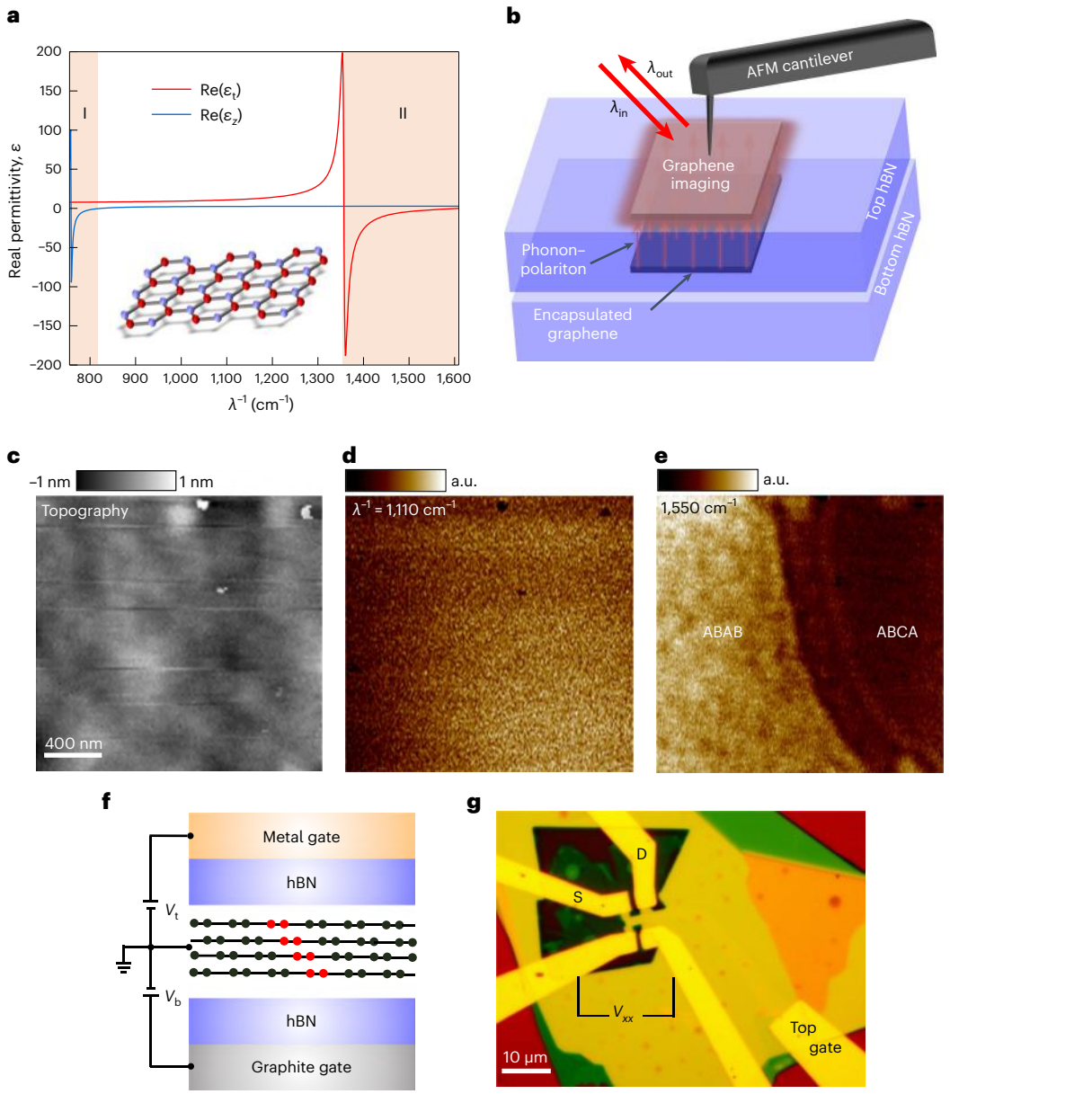

Fig. 2 | Phonon–polariton-assisted near-field optical imaging of graphene stacking orders under hBN coverage. a, Derived real part of the permittivity tensor components of hBN. Type-I lower and type-II upper Reststrahlen bands are shaded. The inset shows a schematic of the hBN crystal structure. **b**, Illustration of the phonon–polariton-assisted near-field optical imaging measurement of graphene encapsulated by hBN. Infrared light (red arrows) at a certain wavenumber within the hBN Reststrahlen band is focused onto the apex of a metal-coated AFM tip. The phonon–polaritons (orange arrows) propagate onto the top hBN surface, are scattered by the AFM tip and detected by an mercury cadmium telluride detector in the far field. **c**–**e**, Topography (**c**) and SNOM images when incident wavenumbers (λ^{-1}) of the hBN-encapsulated tetralayer graphene are 1,110 cm^{-1} (**d**) and 1,550 cm^{-1} (**e**). **f**, Schematic of the side view of the dual-gated hBN/ABCA-4LG/hBN Hall bar device. One unit cell of ABCA-4LG is labelled in red. **g**, Optical image of the final dual-gated hBN/ABCA-4LG/hBN Hall bar device. For transport measurements, we applied current *I* through the source (S) and drain (D), and measured the voltage V_{xx}.

plausible candidate is the LAF state with broken time-reversal symmetry. We also performed mean-field Hartree–Fock (HF) calculations, and find that the LAF phase is energetically favourable than the Fi and F phases at $D = 0$, and the phase transition from LAF to the Fi and F phases occurs as the electric fields are gradually increased (Methods and Extended Data Fig. 5d–g).

The LAF insulator state is further supported by our magneto-transport measurements. We investigate the resistivity at $n = D = 0$ under an in-plane magnetic field $B_\parallel$ and an out-of-plane magnetic field $B_\perp$. Figure 3d shows that the resistivity and gap remain largely unchanged by $B_\parallel$ (Extended Data Fig. 4 shows additional data) and experience a significant drop with $B_\perp$. Since $B_\parallel$ and $B_\perp$ have the same effect on spin, the observed decrease in the gap under $B_\perp$ is attributed to the influence on the valley degree of freedom. To explain this behaviour, we construct a gap diagram (Fig. 3e) based on the LAF state. In the presence of $B_\perp$, the valley can be illustrated following the LAF state. Under $B_\perp$, the valley Zeeman splitting leads to a reduction in the LAF gap by $g_v \mu B_\perp$, where g_v represents the valley *g*-factor and μ represents the Bohr magneton. Analysing the measurement results (Fig. 3d), we find that the reduction in gap is approximately 11 meV at 12 T. This allows us to estimate the value of g_v to be around 20, which is consistent with previous experimental findings in graphene[30]. We note that the gap should reduce by 1.2 meV, about 8% of the original gap size, when $B_\parallel = 12$ T if considering a smaller *g*-factor of spin. We did not observe

https://doi.org/10.1038/s41565-023-01558-1

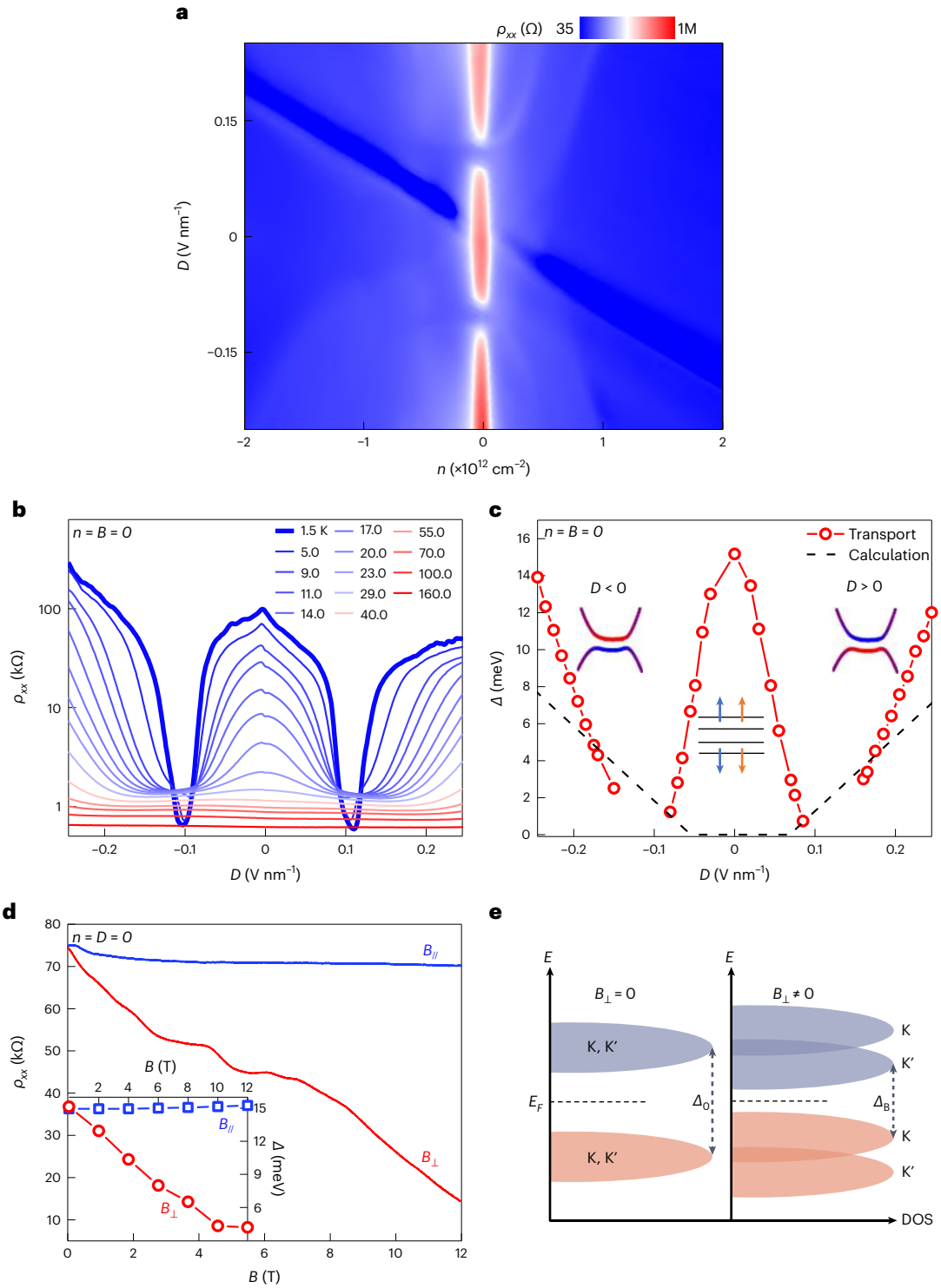

Fig. 3 | Broken-symmetry insulators at $n = 0$. **a**, Colour plot of resistivity ρ_{xx} as a function of carrier density n and displacement field D. The colour bar is in the log scale. **b**, D-dependent ρ_{xx} for $n = 0$ at varied temperatures from 1.5 to 160.0 K. **c**, D-dependent transport gap (red circles) extracted from the Arrhenius plot in **b** and calculated single-particle gap (dashed line). The calculated gap size is reduced by a factor of 5.6 considering the screening in graphene. The inset at $D = 0$ illustrates the isospin flavour distribution of the LAF state, the four black lines represent ABCA-4LG, the arrows represent spins and the two colours represent two valleys. The insets on the two sides are band structures colour coded with red and blue, respectively, denoting wave functions in the top and bottom two layers. **d**, Resistivity as a function of in-plane and out-of-plane magnetic fields. The inset shows the extracted transport gaps at different magnetic fields. **e**, Illustration of the LAF insulator and its valley Zeeman splitting in the out-of-plane magnetic field.

this reduction possibly due to the limitation on the accuracy of the transport-extracted gap.

The observation of the LAF insulator state has been reported in suspended bilayer[25,31], trilayer[12] and multilayer rhombohedral graphene[13,32]. However, in graphene on hBN, the bilayer and ABC trilayer do not exhibit such an insulating state, possibly due to the screening effect from the hBN dielectric environment. In the case of ABCA-4LG, the strong Coulomb interactions are sufficient to drive the emergence of

https://doi.org/10.1038/s41565-023-01558-1

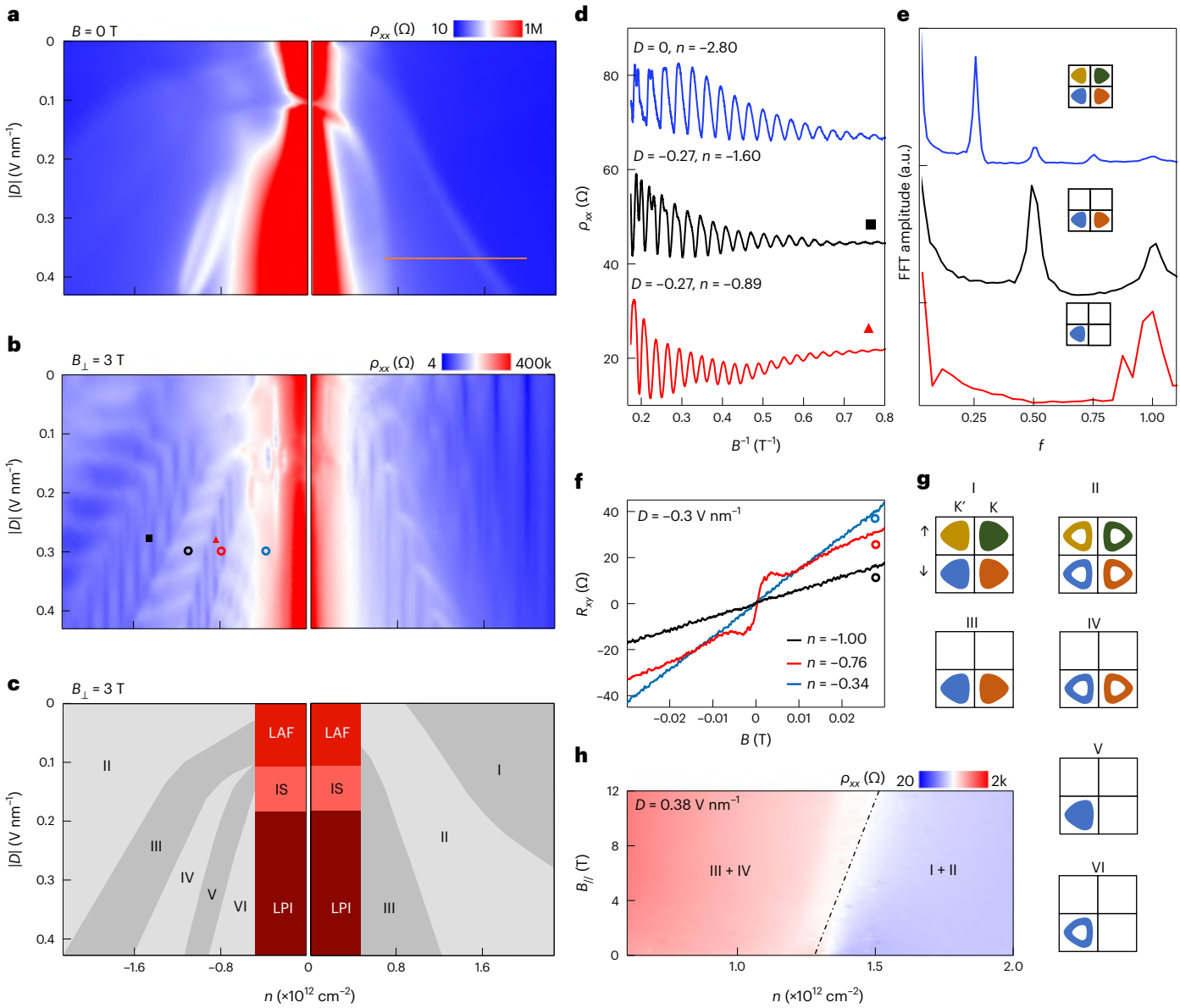

Fig. 4 | Broken-symmetry metals in ABCA-4LG. a,**b**, The n–D colour plot of resistivity at $B = 0$ T (**a**) and $B = 3$ T (**b**). The colour bars are linear in **a** and logarithmic in **b**. **c**, Experimental phase diagram of the broken-symmetry states. IS, intermediate state. **d**, Shubnikov–de Haas oscillations at normal, SP and SVP metal states. The data of SP and SVP metals are taken at the square (black) and triangle (red) in **b**. **e**, Fast Fourier transformation (FFT) analysis of the quantum oscillations in **d**. The inset shows the corresponding Fermi surface contours of the three metals. **f**, Hall resistivity R_{xy} as a function of magnetic field measured at the black, red and blue circles in **b**. All the data were obtained at $T = 1.5$ K. **g**, Schematic of the Fermi surface contours of each phase defined in **c**. The filled colours represent the spin and valley flavours, and the inset in **e** follows the same convention. **h**, The n–$B_{\parallel}$ colour plot of resistivity at $D = 0.38$ V nm^{-1}. The data are taken along the horizontal orange line in **a**.

the LAF state. The reproducibility of the LAF state in hBN-encapsulated ABCA-4LG is evident, as similar behaviours are observed in multiple devices (Extended Data Figs. 7 and 8). There is no transport signature of the moiré superlattice between ABCA-4LG and hBN in all the devices considered in this study, ruling out possible effects originating from hBN alignment. The LAF gap in a ten-layer rhombohedral graphene device was reported to be 2–3 meV (ref. 32), significantly less than that of ABCA-4LG, indicating interesting layer-dependent Coulomb interactions. It is worth noting that the magnetic field dependence of the LAF state in our study is opposite to that observed in suspended graphene. In the suspended samples, the LAF gap increases with $B_{\perp}$ (refs. 12,13,25,31). The contrasting magnetic field dependence observed in these two different sample structures raises intriguing questions for further investigation.

Broken-symmetry metals

Doping in ABCA-4LG can lead to interaction-driven broken symmetries for itinerant carriers, potentially resulting in spontaneous spin and/or valley polarizations through a different mechanism, following the Stoner criterion, that is, $D(E_F)U > 1$, where $D(E_F)$ is the DOS at Fermi energy E_F and U is the Coulomb energy[33], compared with the insulating states at CNP. In ABCA-4LG, on doping, U is typically large and $D(E_F)$ at the VHS can be further tuned by D, providing a tunable platform of Stoner ferromagnetism. It was argued that the non-local exchange between electrons favours the formation of electron or hole pockets of nearby electrons in k space[34], leading systems with finite D and carrier densities to the so-called momentum-space exchange condensation that favours spontaneous spin–valley flavour polarization with an

eventual onset of nematic broken-rotational-symmetry phases. In Fig. 4a, due to the presence of p–n junctions formed by misalignment between the top and bottom gates at opposite signs (which leads to bad contact resistance), our focus is on the resistivities in the hole side at negative D and the electron side at positive D. The metallic regions with distinct behaviours are separated by resistivity bumps, indicated by the white lines (representing resistivity humps) in Fig. 4a. In a perpendicular magnetic field of $B = 3$ T, Landau levels with different degeneracies are developed (Fig. 4b).

To further investigate the degeneracies in different regions, in Fig. 4d, we performed the direct measurements of quantum oscillations as a function of the perpendicular magnetic field B, and fixing the values of n and D in three different regions. Figure 4e shows the fast Fourier transformation of the quantum oscillations in Fig. 4d, clearly revealing one dominant peak for each region, located at $f = 1/4$, 1/2 and 1. These frequencies correspond to fourfold, twofold and onefold degenerate bands, respectively. In graphene, the expected Landau-level degeneracy is typically 4, considering the degeneracy of spin and valley. However, the observed degeneracies of 1 and 2 indicate a spin-and-valley-polarized (SVP) state and a spin-polarized (SP) state, respectively[34,35]. The anomalous Hall signal (Fig. 4f, red curve) serves as the signature of valley polarization in the SVP metallic state. The spin polarization is supported by Fig. 4h, where the SP metallic state is stabilized, and its phase boundary shifts to higher densities under an in-plane magnetic field. For comparison, as expected, the boundary between the SP and SVP states exhibits no dependence on the in-plane magnetic field (Extended Data Fig. 9). The Landau levels between different polarized states are represented by slanted lines, indicating that the Landau levels simultaneously depend on both n and D. These regions correspond to the presence of electron and hole Fermi pockets, illustrated as II, IV and VI (Fig. 4g).

Figure 4c summarizes our experimental discoveries, presenting the broken-symmetry phase diagram of ABCA-4LG as a function of n and D:

1. At $n = D = 0$, the strong Coulomb interactions result in the breaking of time-reversal symmetry and the formation of an LAF insulator.
2. At large D, the broken sublattice inversion symmetry leads to LPI.
3. Between LAF and LPI, there exists a low-resistivity intermediate state.
4. At $n \neq 0$ and $D \neq 0$, the Coulomb interactions break the spin and valley degeneracies, giving rise to the development of spontaneous Stoner F metal phases, namely, the SVP and SP metallic states. The Fermi surfaces corresponding to each of the broken-symmetry metallic phases are illustrated in Fig. 4g. The phase boundaries of the SP and SVP regions can also be clearly identified in the Landau-level fan diagram (Extended Data Fig. 10).

Conclusions

Through a comparative analysis between our observations of the LAF state in ABCA-4LG and other experimental findings in related rhombohedral graphene multilayers (suspended AB bilayer[11,25,31], ABC trilayer[12], ABCA-4LG (ref. 13) and other examples[36–38]), several intriguing distinct behaviours have emerged, which merit further investigation. First, we note the divergent magnetic field dependencies of the LAF gap between suspended rhombohedral graphene and graphene on hBN, which is a noteworthy contrast. Secondly, the layer dependence of the LAF state is of particular interest. It initially emerges in tetralayer, strengthens in pentalayer, experiences gradual attenuation in thickness ranging from 3.3 to 4.0 nm and ultimately vanishes in thicker multilayers. Last, a significant question arises regarding the potential existence of superconductivity in ABCA-4LG, given its similarities with AB bilayer and ABC trilayer in terms of SVP states, which presents an exciting avenue for further exploration.

Note added in proof: We recently became aware of a related work on pentalayer graphene describing correlated insulators and Chern insulators[38].

Online content

Any methods, additional references, Nature Portfolio reporting summaries, source data, extended data, supplementary information, acknowledgements, peer review information; details of author contributions and competing interests; and statements of data and code availability are available at https://doi.org/10.1038/s41565-023-01558-1.

References

1. Min, H., Borghi, G., Polini, M. & MacDonald, A. H. Pseudospin magnetism in graphene. *Phys. Rev. B* **77**, 041407 (2008).
2. Zhang, F., Min, H., Polini, M. & MacDonald, A. H. Spontaneous inversion symmetry breaking in graphene bilayers. *Phys. Rev. B* **81**, 041402 (2010).
3. Nandkishore, R. & Levitov, L. Quantum anomalous Hall state in bilayer graphene. *Phys. Rev. B* **82**, 115124 (2010).
4. Zhang, F., Jung, J., Fiete, G. A., Niu, Q. & MacDonald, A. H. Spontaneous quantum Hall states in chirally stacked few-layer graphene systems. *Phys. Rev. Lett.* **4**, 156801 (2011).
5. Vafek, O. & Yang, K. Many-body instability of Coulomb interacting bilayer graphene: renormalization group approach. *Phys. Rev. B* **81**, 041401 (2010).
6. Zhang, Y. et al. Landau-level splitting in graphene in high magnetic fields. *Phys. Rev. Lett.* **96**, 136806 (2006).
7. Cao, Y. et al. Unconventional superconductivity in magic-angle graphene superlattices. *Nature* **556**, 43–50 (2018).
8. Cao, Y. et al. Correlated insulator behaviour at half-filling in magic-angle graphene superlattices. *Nature* **556**, 80–84 (2018).
9. Zondiner, U. et al. Cascade of phase transitions and Dirac revivals in magic-angle graphene. *Nature* **582**, 203–208 (2020).
10. Wong, D. et al. Cascade of electronic transitions in magic-angle twisted bilayer graphene. *Nature* **582**, 198–202 (2020).
11. Velasco, J. Transport spectroscopy of symmetry-broken insulating states in bilayer graphene. *Nat. Nanotechnol.* **7**, 156–160 (2012).
12. Lee, Y. et al. Competition between spontaneous symmetry breaking and single-particle gaps in trilayer graphene. *Nat. Commun.* **5**, 5656 (2014).
13. Myhro, K. et al. Large tunable intrinsic gap in rhombohedral-stacked tetralayer graphene at half filling. *2D Mater.* **5**, 045013 (2018).
14. Chen, G. et al. Signatures of tunable superconductivity in a trilayer graphene moiré superlattice. *Nature* **572**, 215–219 (2019).
15. Chen, G. et al. Tunable correlated Chern insulator and ferromagnetism in a moiré superlattice. *Nature* **579**, 56–61 (2020).
16. Koshino, M. Interlayer screening effect in graphene multilayers with ABA and ABC stacking. *Phys. Rev. B* **81**, 125304 (2010).
17. Aoki, M. & Amawashi, H. Dependence of band structures on stacking and field in layered graphene. *Solid State Commun.* **142**, 123–127 (2007).
18. Zhang, F., Sahu, B., Min, H. & MacDonald, A. H. Band structure of ABC-stacked graphene trilayers. *Phys. Rev. B* **82**, 035409 (2010).
19. Kerelsky, A. et al. Moiréless correlations in ABCA graphene. *Proc. Natl Acad. Sci. USA* **118**, e2017366118 (2021).
20. Ju, L. et al. Topological valley transport at bilayer graphene domain walls. *Nature* **520**, 650–655 (2015).
21. Chen, G. et al. Evidence of a gate-tunable Mott insulator in a trilayer graphene moiré superlattice. *Nat. Phys.* **15**, 237–241 (2019).
22. Caldwell, J. D. et al. Sub-diffractional volume-confined polaritons in the natural hyperbolic material hexagonal boron nitride. *Nat. Commun.* **5**, 5221 (2014).

23. Dai, S. et al. Subdiffractional focusing and guiding of polaritonic rays in a natural hyperbolic material. *Nat. Commun.* **6**, 6963 (2015).
24. Li, H. et al. Electrode-free anodic oxidation nanolithography of low-dimensional materials. *Nano Lett.* **18**, 8011–8015 (2018).
25. Weitz, R. T., Allen, M. T., Feldman, B. E., Martin, J. & Yacoby, A. Broken-symmetry states in doubly gated suspended bilayer graphene. *Science* **330**, 812–816 (2010).
26. Zhang, Y. et al. Direct observation of a widely tunable bandgap in bilayer graphene. *Nature* **459**, 820–823 (2009).
27. Maher, P. et al. Evidence for a spin phase transition at charge neutrality in bilayer graphene. *Nat. Phys.* **9**, 154–158 (2013).
28. Jung, J. & MacDonald, A. H. Gapped broken symmetry states in ABC-stacked trilayer graphene. *Phys. Rev. B* **88**, 075408 (2013).
29. Jung, J., Zhang, F. & MacDonald, A. H. Lattice theory of pseudospin ferromagnetism in bilayer graphene: competing interaction-induced quantum Hall states. *Phys. Rev. B* **83**, 115408 (2011).
30. Xiao, D., Yao, W. & Niu, Q. Valley contrasting physics in graphene: magnetic moment and topological transport. *Phys. Rev. Lett.* **99**, 236809 (2007).
31. Feldman, B. E. Broken-symmetry states and divergent resistance in suspended bilayer graphene. *Nat. Phys.* **5**, 889–893 (2009).
32. Shi, Y. et al. Electronic phase separation in multilayer rhombohedral graphite. *Nature* **584**, 210–214 (2020).
33. Stoner, E. C. Collective electron ferromagnetism. *Proc. R. Soc. Lond. A* **165**, 372–414 (1997).
34. Zhou, H. et al. Half- and quarter-metals in rhombohedral trilayer graphene. *Nature* **598**, 429–433 (2021).
35. de la Barrera, S. C. et al. Cascade of isospin phase transitions in Bernal-stacked bilayer graphene at zero magnetic field. *Nat. Phys.* **18**, 771–775 (2022).
36. Zhou, H., Xie, T., Taniguchi, T., Watanabe, K. & Young, A. F. Superconductivity in rhombohedral trilayer graphene. *Nature* **598**, 434–438 (2021).
37. Zhou, H. et al. Isospin magnetism and spin-polarized superconductivity in Bernal bilayer graphene. *Science* **375**, 774–778 (2022).
38. Han, T. et al. Correlated insulator and Chern insulators in pentalayer rhombohedral-stacked graphene. *Nat. Nanotechnol.* https://doi.org/10.1038/s41565-023-01520-1 (2023).

Methods

Sample fabrications

Graphene, graphite and hBN are mechanically exfoliated on SiO_2 (285 nm)/Si substrates, and the layer numbers are identified using optical contrast and AFM measurements. The stacking order of trilayer and tetralayer graphene is identified using SNOM and Raman spectroscopy. A dry transfer method using polypropylene carbonate or polycarbonate is implemented to construct the heterostructures. During transfer, graphene and hBN are not specially aligned to certain twisted angles. Standard electron-beam lithography, reactive ion etching and metal evaporation are conducted to make the devices into Hall bar geometry with one-dimensional edge contacts. After each step of transfer and fabrications, SNOM imaging is performed to check the stacking orders of graphene.

Phonon–polariton-assisted near-field optical imaging

The key factor that enables the penetration imaging of embedded graphene across the hBN flake is the hyperbolic nature of the hBN crystal. In the Reststrahlen band between 1,370 and 1,610 cm^{-1}, the real part of the in-plane permittivity (ε_t) of hBN is negative, whereas that of the out-of-plane permittivity (ε_z) is positive. As a result, hBN supports hyperbolic phonon–polaritons that mainly propagate along a specific direction at a fixed angle θ with respect to the z axis as $\theta = \arctan(i\sqrt{\epsilon_t}/\sqrt{\epsilon_z})$, determined by the hyperbolic dielectric function. The advantage of directional polaritonic rays is the greatly enhanced propagation length, due to a reduced radical spreading loss. A previous study reported subdiffractional focusing and guiding of the polaritonic rays in hBN (ref. 23). Here, in our experiment, the directionally propagating polaritonic rays carry the underneath graphene domain patterns to the hBN top surface, which were finally coupled out by the metallic AFM tip and recorded by a mercury cadmium telluride detector placed in the far field. As the ABAB graphene domain typically possesses larger optical conductivity than ABCA graphene, we can identify it from its near-field optical response by scanning it even with an hBN coverage. Moreover, SNOM imaging enables a high resolution down to 10 nm, which can considerably enhance the precision in device fabrication. As a result, the phonon–polariton-assisted imaging method can efficiently help identify the graphene stacking order after the transfer process and push the rhombohedral-graphene-related devices to a more applicable level.

Transport measurements

The transport measurement is done in the 1.5-K-base-temperature Oxford variable-temperature insert system. Stanford Research Systems SR830 and SR860 and Guangzhou Sine Scientific Instrument OE1201 lock-in amplifiers with an alternating current of 10 nA at a frequency of 17 Hz in combination with a 100 MΩ resistor are used to measure the resistivity. A Keithley 2400 source meter is used to apply the gate voltages. The displacement field D is set by $D = (D_b + D_t)/2$, and the carrier density is determined by $n = (D_b - D_t)/e$. Here $D_b = +\varepsilon_b(V_b - V_b^0)/d_b$ and $D_t = -\varepsilon_t(V_t - V_t^0)/d_t$, where ε and d are the dielectric constant and thickness of the dielectric layers, respectively; and V_b^0 and V_t^0 are the effective offset voltages caused by environment-induced carrier doping.

Band calculation

The electronic structure of ABCA-stacked multilayer graphene is modelled with a tight-binding Hamiltonian whose hopping terms are fitted to reproduce the density-functional-theory-calculated energy bands obtained within the local density approximation. This Hamiltonian reads

$$H_{4LG} = \begin{pmatrix} H_{11} & H_{12} & H_{13} & H_{14} \\ H_{12}^\dagger & H_{22} & H_{23} & H_{24} \\ H_{13}^\dagger & H_{12}^\dagger & H_{33} & H_{34} \\ H_{14}^\dagger & H_{24}^\dagger & H_{34}^\dagger & H_{44} \end{pmatrix},$$

where $(H_{ll})_{2\times2}$ represent the intralayer graphene Hamiltonian diagonal blocks for layers $l = 1, 2, 3$ and 4, and the interlayer coupling $(H_{ij})_{2\times2}$ ($i \neq j = 1, 2, 3$) terms near the Dirac points are respectively given as follows:

$$H_{ll}(\mathbf{k}) = \begin{pmatrix} u_{A_l} & v_0\pi^\dagger \\ v_0\pi & u_{B_l} \end{pmatrix} + V_{ll}\mathbb{I},\ H_{12}(\mathbf{k}) = \begin{pmatrix} -v_4\pi^\dagger & -v_3\pi \\ t_1 & -v_4\pi^\dagger \end{pmatrix},\ H_{13}(\mathbf{k}) = \begin{pmatrix} 0 & t_2 \\ 0 & 0 \end{pmatrix}$$

Here $\pi = (vp_x + ip_y)$ depends on the valley index $v = \pm1$ where the momentum is measured from the Dirac points $K_v = (v\frac{4\pi}{3a}, 0)$, and for each valley. The positive-valued parameters associated with the hopping terms are $v_i = \sqrt{3}a|t_i|/2\hbar$ and the term $V_{ll}\mathbb{I}$ is used to define the potential of each layer. We model the drop in interlayer potential Δ between consecutive layers due to a perpendicular electric field through $V = \Delta(\frac{3}{2}, \frac{1}{2}, -\frac{1}{2}, -\frac{3}{2})$. The hopping parameters used in this work, namely, $(t_0, t_1, t_2, t_3, t_4) = (-2.6000, 0.3561, -0.0093, 0.2930, 0.1440)$ eV, are similar to those in another work[39] that are the corresponding nearest-neighbour intralayer hopping terms between A_l and B_l sites and interlayer B_l and A_{l+1}, A_l and B_{l+2}, A_l and B_{l+1} and A_l (B_l) and (A_{l+1}) B_{l+1} sites (Extended Data Fig. 5a). The diagonal-site potentials u_{A_l} (u_{B_l}) at each sublattice of 4LG are $u_{A_1} = u_{B_4} = 0, u_{B_1} = u_{A_4} = 0.0122$ eV, $u_{A_2/A_3} = u_{B_2/B_3} = -0.0164$ eV.

Spontaneous degeneracy breaking

We carry out a self-consistent HF calculation in the sublattice-spin basis $\lambda = (\kappa, \sigma)$, where $\kappa = \{A_1, B_1, A_2, B_2, A_3, B_3, A_4, B_4\}$ for the sublattice-site labels and $\sigma = \{\uparrow, \downarrow\}$ for up/down spins. The HF Coulomb term V_{HF} to be added in the band Hamiltonian H_{4LG} can be written as

$$V_{HF} = \sum_{\mathbf{k},\lambda,\lambda'} \sum_{\mathbf{k}'} \big[\langle \mathbf{k}\lambda\mathbf{k}'\lambda'|V|\mathbf{k}\lambda\mathbf{k}'\lambda'\rangle\langle c_{\mathbf{k}'\lambda}^\dagger c_{\mathbf{k}'\lambda}\rangle c_{\mathbf{k}\lambda}^\dagger c_{\mathbf{k}\lambda} - \langle \mathbf{k}\lambda\mathbf{k}'\lambda'|V|\mathbf{k}'\lambda\mathbf{k}\lambda'\rangle\langle c_{\mathbf{k}'\lambda'}^\dagger c_{\mathbf{k}'\lambda}\rangle c_{\mathbf{k}\lambda}^\dagger c_{\mathbf{k}\lambda'}\big],$$

where the details of the calculations closely follow those from previous works[28,29]. Here we have chosen $\mathbf{k}$-point densities near the valleys equivalent to 576 × 576 and a relative permittivity of $\varepsilon_r = 4$.

We define the energy terms based on the unrestricted HF equations[40], where the total energy (E_{tot}) consists of the tight-binding (E_{band}), Hartree (E_H) and exchange (E_X) energy terms as follows:

$$E_{tot} = E_{band} + E_H + E_X,$$

$$E_H = \frac{1}{2}\sum_{\kappa\kappa'}\sum_{\mathbf{k}\sigma}\sum_{\mathbf{k}'\sigma'}\langle \mathbf{k}(\kappa,\sigma)\mathbf{k}'(\kappa',\sigma')|V|\mathbf{k}(\kappa,\sigma)\mathbf{k}'(\kappa',\sigma')\rangle\langle c_{\mathbf{k}'(\kappa',\sigma')}^\dagger c_{\mathbf{k}'(\kappa',\sigma')}\rangle\langle c_{\mathbf{k}(\kappa,\sigma)}^\dagger c_{\mathbf{k}(\kappa,\sigma)}\rangle,$$

$$E_X = -\frac{1}{2}\sum_{\kappa\kappa'}\sum_{\mathbf{k}\sigma}\sum_{\mathbf{k}'\sigma'}\langle \mathbf{k}(\kappa,\sigma)\mathbf{k}'(\kappa',\sigma')|V|\mathbf{k}(\kappa,\sigma)\mathbf{k}'(\kappa',\sigma')\rangle\langle c_{\mathbf{k}'(\kappa',\sigma')}^\dagger c_{\kappa'(\kappa,\sigma)}\rangle\langle c_{\mathbf{k}(\kappa,\sigma)}^\dagger c_{\mathbf{k}(\kappa',\sigma')}\rangle\delta_{\sigma\sigma'},$$

$$E_{band} = (\sum_{\mathbf{nk}\sigma}\epsilon_{\mathbf{nk}\sigma}\langle c_{\mathbf{nk}\sigma}^\dagger c_{\mathbf{nk}\sigma}\rangle) - 2(E_H + E_X).$$

The first term in E_{band} is the orbital energy defined by the eigenenergies $\varepsilon_{\mathbf{nk}\sigma}$ and eigenstates $|\mathbf{nk}\sigma\rangle$ over the band index $\mathbf{n}$, $\mathbf{k}$ points and spin σ.

We could classify the different ground states as the spin–valley flavour AF phase with equal charge polarization at opposite surface layers, the flavour Fi with partially unbalanced layer-charge polarizations and flavour F states with the maximum charge polarization difference between the top and bottom layers[1,29].

In Extended Data Fig. 5b, we show a schematic of the layer polarization for each phase, where two of the four spin–valley flavours polarize the states to the top layer in the AF phases, which includes quantum anomalous Hall and LAF, three for Fi and four for F phases. We note that the Fi phase is an intriguing one with simultaneously associated spin, charge and valley Hall conductivities.

Within HF theory for charge-neutral bilayer[29] and trilayer[28], it was shown that AF phases, especially the LAF phase, are energetically preferred over Fi and F phases at zero electric field. The application

of a perpendicular electric field leads to phase transitions from the charge-balanced AF to the unbalanced Fi and F phases.

To examine the ground states for the charge-neutral ABCA-4LG system, we compare the total energies for each phase, where we have used a 576 × 576 k-point mesh grid near two Dirac points, namely, K and K′, and 18 × 18 k-point grid for the rest of the first Brillouin zone (Extended Data Fig. 5c).

We verified that the charge-neutral ABCA-4LG system also shows that the LAF phase is energetically favourable than the Fi and F phases in the absence of an external electric field, and the phase transition from the LAF to the Fi and F phases occur when the electric fields are gradually increased.

In Extended Data Fig. 5d–g, we illustrate the electric-field-dependent variations for all the four phases on the bandgap, total energy, band and Hartree energy, and exchange energy.

Data availability

The data shown in Figs. 1, 2 and 4 are available from the Harvard Dataverse Repository at https://doi.org/10.7910/DVN/SU00ZW. The datasets generated during and/or analysed during this study are available from the corresponding authors upon reasonable request.

Code availability

The code shown in Fig. 1b–d,f,g to generate band structures is available from the Harvard Dataverse Repository at https://doi.org/10.7910/DVN/SU00ZW.

References

39. Park, Y., Kim, Y., Chittari, B. L. & Jung, J. Topological flat bands in rhombohedral tetralayer and multilayer graphene on hexagonal boron nitride moiré superlattices. *Phys. Rev. B* **108**, 155406 (2023).
40. Szabo, A. & Ostlund, N. S. *Modern Quantum Chemistry: Introduction to Advanced Electronic Structure Theory* 1st edn (Dover Publications, 1996).

Acknowledgements

We acknowledge helpful discussions with J. Liu, S. Wang, Y. Zhang and F. Wang. This work is supported by the National Key Research Program of China (grant nos. 2020YFA0309000, 2021YFA1400100, 2021YFA1202902 and 2022YFA1402401), NSF of China (grant nos.12174248 and 12074244) and SJTU no. 21X010200846. G.C. acknowledges sponsorship from the Yangyang Development Fund. K.W. and T.T. acknowledge support from the JSPS KAKENHI (grant nos. 20H00354, 21H05233 and 23H02052) and World Premier International Research Center Initiative (WPI), MEXT, Japan.

Author contributions

G.C. supervised the project. K.L. and J.Z. fabricated the devices and performed the transport measurements with the assistance of Y.S. and B.L. K.L. and Z.S. performed the near-field infrared and AFM measurements. K.L., F.L., Y.R., Y.P., W.L. and J. Jung calculated the band structures. K.W. and T.T. grew the hBN single crystals. K.L., J.Z., Y.S., J. Jung and G.C. analysed the data. K.L., Z.S., J. Jung and G.C. wrote the paper with input from all authors.

Competing interests

The authors declare no competing interests.

Additional information

Extended data is available for this paper at https://doi.org/10.1038/s41565-023-01558-1.

Supplementary information The online version contains supplementary material available at https://doi.org/10.1038/s41565-023-01558-1.

Correspondence and requests for materials should be addressed to Jeil Jung or Guorui Chen.

Peer review information *Nature Nanotechnology* thanks Yuan Cao and the other, anonymous, reviewer(s) for their contribution to the peer review of this work.

https://doi.org/10.1038/s41565-023-01558-1

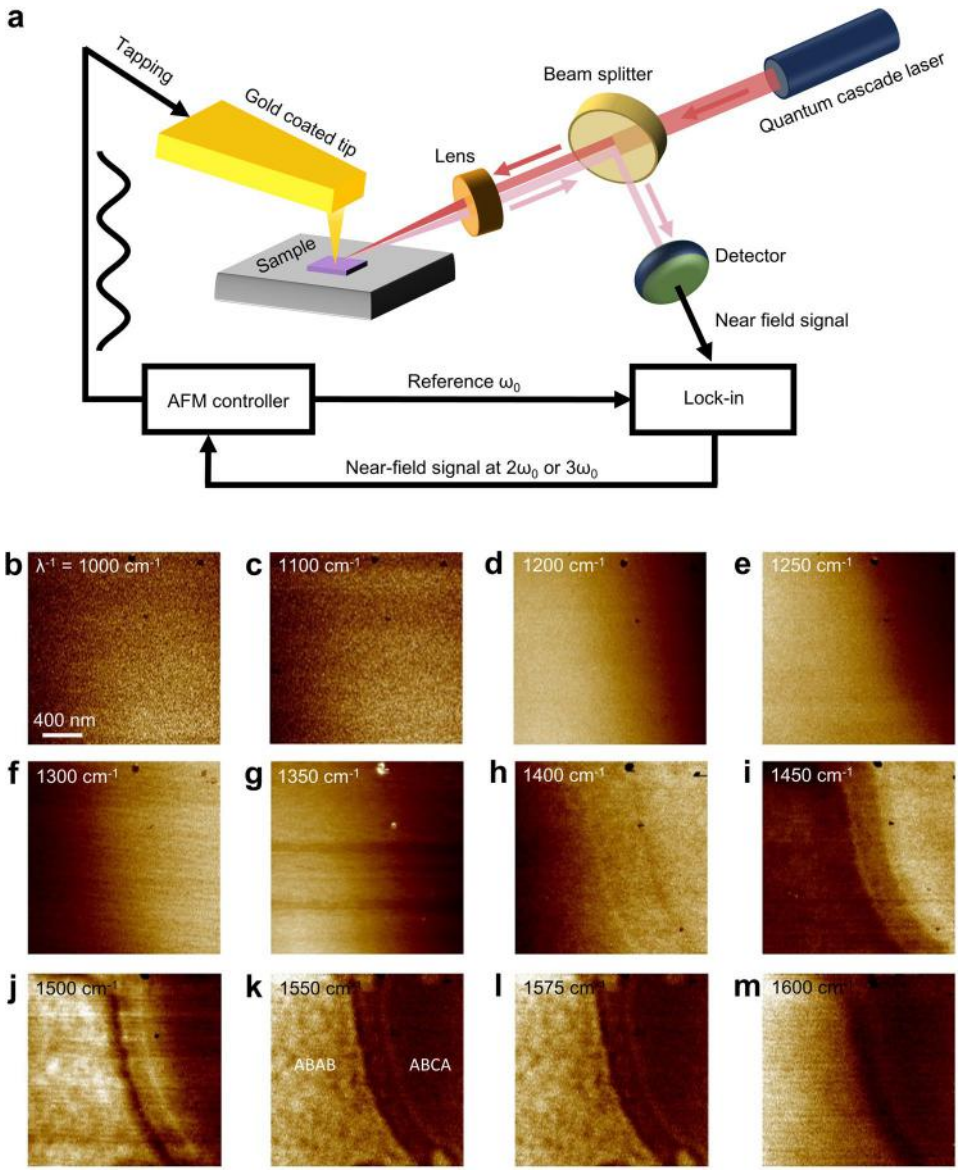

Extended Data Fig. 1 | Wavelength dependent SNOM contrast of ABCA and ABAB regions. a, Schematic diagram of a scattering-type scanning near-field optical microscope (s-SNOM). The wavelength of quantum cascade laser is tunable from 900 to 1675 cm^{-1}, allowing us to find a best wavelength for the phonon-polariton assisted infrared imaging of graphene under hBN. The beam splitter and lens are both made of ZnSe, and the scattered light signal is collected by an HgCdTe detector working at liquid nitrogen temperature in the far field. **b**–**m**, IR-SNOM images of the same tetra-layer graphene sample with that in Fig. 2c–e at different incident wavelength ranging from 1000 to 1600 cm^{-1}. Only when the incident wavelength lies in the hBN Reststrahlen (1370 ~ 1610 cm^{-1}), ABAB and ABCA regions can be clearly distinguished. Between 1500 ~ 1600 cm^{-1}, ABCA is always darker than ABAB (j ~ m), between 1400 ~ 1500 cm^{-1}, ABAB should be darker (Fig. h, i). Below 1350 cm^{-1} there is no obvious boundary between ABCA and ABAB and the contrast is weak. The hBN thickness is about 35 nm.

https://doi.org/10.1038/s41565-023-01558-1

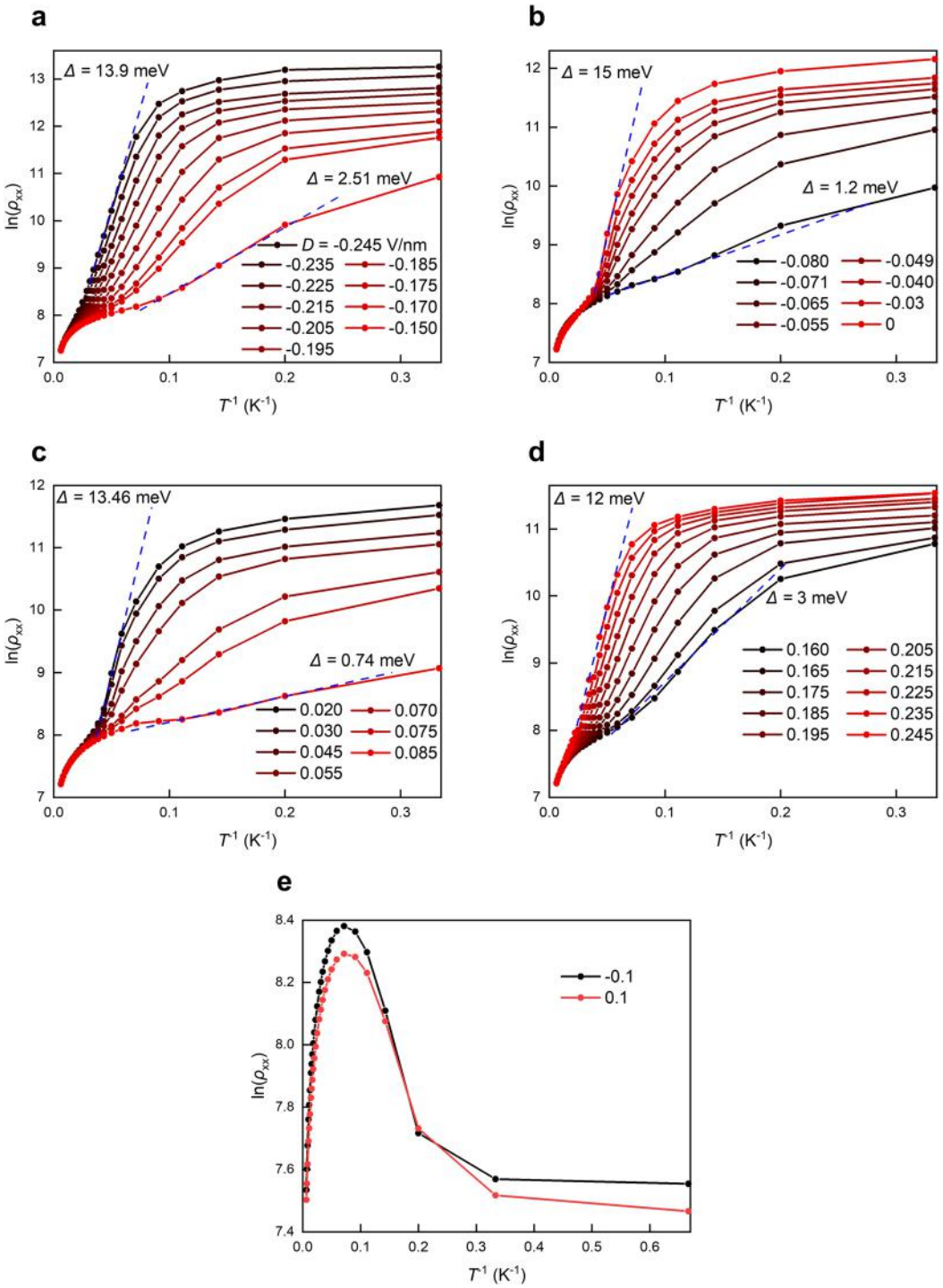

Extended Data Fig. 2 | Arrhenius plot. $\ln(\rho_{xx})$ versus temperature at different displacement fields. The transport gap Δ in Fig. 3c is extracted according to thermal activation equation $\rho_{xx} \propto e^{-\Delta/2k_BT}$. The dashed lines in **a** to **d** represent the linear regions to estimate the gap. **a** and **d** correspond to LPI, **b** and **c** correspond to LAF, **e** corresponds to IS which shows the metallic behavior when temperature is lower than 14 K.

https://doi.org/10.1038/s41565-023-01558-1

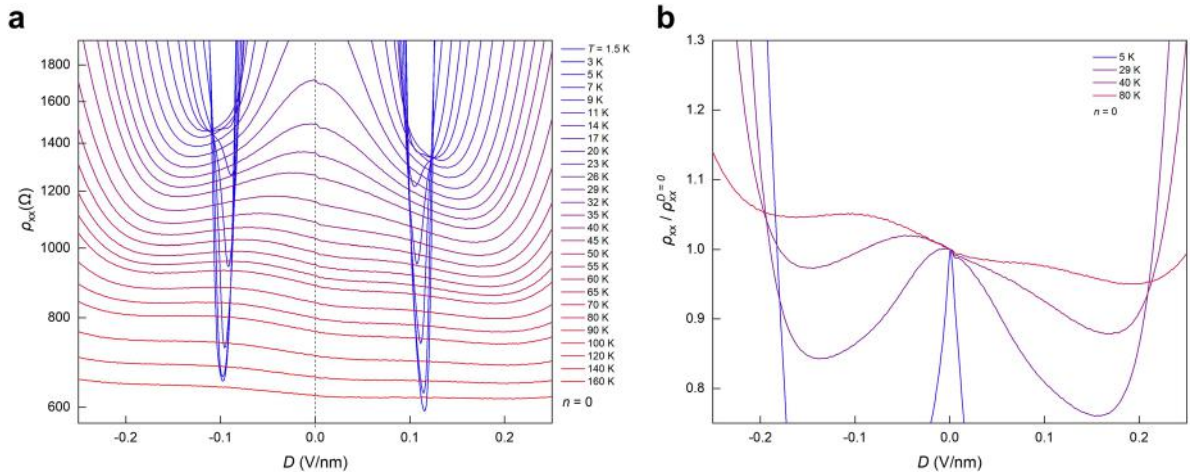

Extended Data Fig. 3 | A possible phase transition. a, Zoomed-in plot of resistivity ρ_{xx} as a function of displacement field D at various temperatures for the device shown in the main text. **b**, Normalized resistivity $\rho_{xx}/\rho_{xx}^{D=0}$ as a function of D at typical temperatures, where $\rho_{xx}^{D=0}$ is the resistivity when $D = 0$.

https://doi.org/10.1038/s41565-023-01558-1

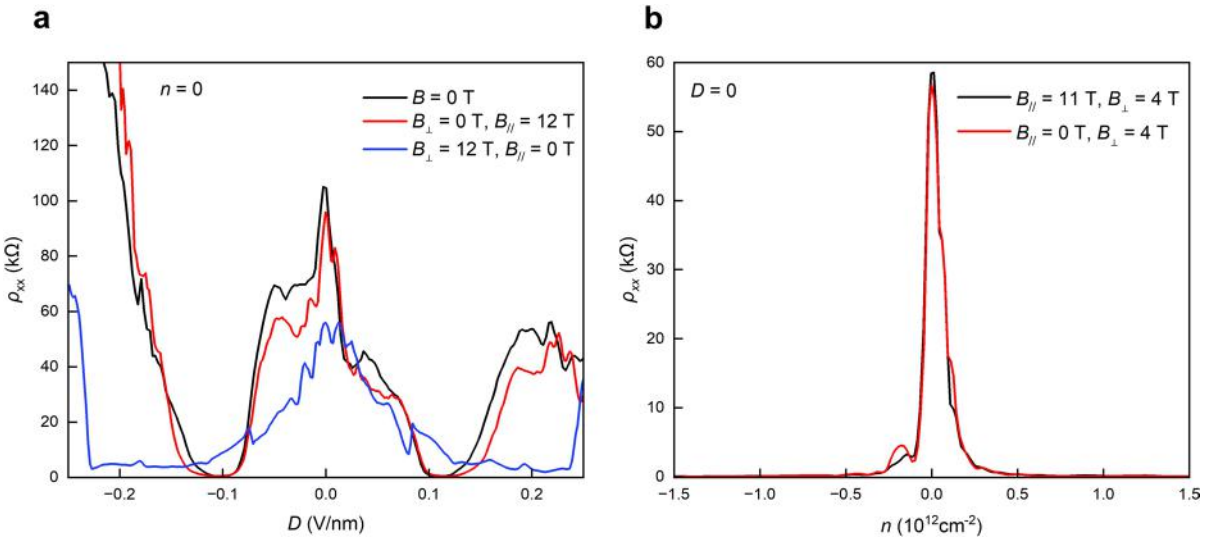

Extended Data Fig. 4 | Comparison of the response to the vertical and parallel magnetic field focusing around $D = 0$. a, $\rho_{xx} - D$ plot at $B = 0$ T; $B_{\perp} = 0$ T, $B_{//} = 12$ T and $B_{\perp} = 12$ T, $B_{//} = 0$ T. **b**, $\rho_{xx} - n$ plot at $B_{\perp} = 4$ T, $B_{//} = 11$ T and $B_{\perp} = 4$ T, $B_{//} = 0$ T. Both data show parallel magnetic field have little influence on the correlated insulator state around CNP. A rotating probe is used to relatively change the direction of magnetic field. According to the measurement of Hall resistance, pure in-plane or out of plane magnetic field (error within 0.1°) can be applied to sample.

https://doi.org/10.1038/s41565-023-01558-1

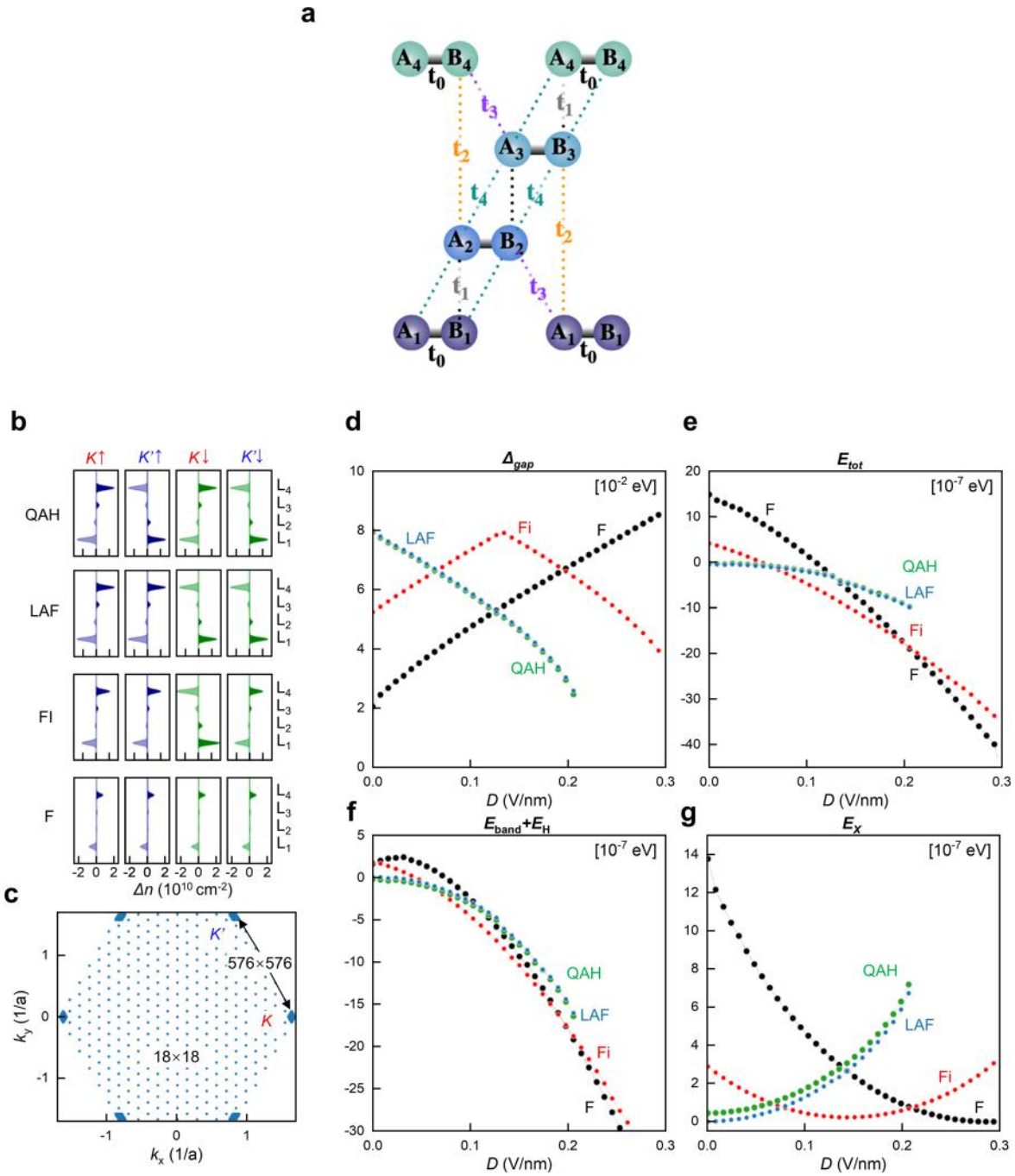

Extended Data Fig. 5 | Hopping parameters and spontaneous degeneracy breaking. a, Illustration of the intralayer and interlayer tight-binding hopping terms of ABCA multilayer graphene used in this work. **b**, Layer resolved distribution of electrons and holes for charge neutral QAH, LAF, and flavor Fi, and F phases illustrating the layer polarization of the four spin-valley flavors ($K\uparrow, K'\uparrow, K\downarrow, K'\downarrow,$). **c**, k-point mesh grid of the first Brillouin zone where the dense grid near two Dirac points, K and K', is equivalent to 576 × 576 k points, and the coarse grid for the rest of the area is to 18 × 18 k points. We show electric field dependent variations on **d** band gap (Δ_{gap}), **e** total energy (E_{tot}), **f** the sum of band (E_{band}) and Hartree (E_H) energy, and **g** exchange energy (E_X) for each phase.

https://doi.org/10.1038/s41565-023-01558-1

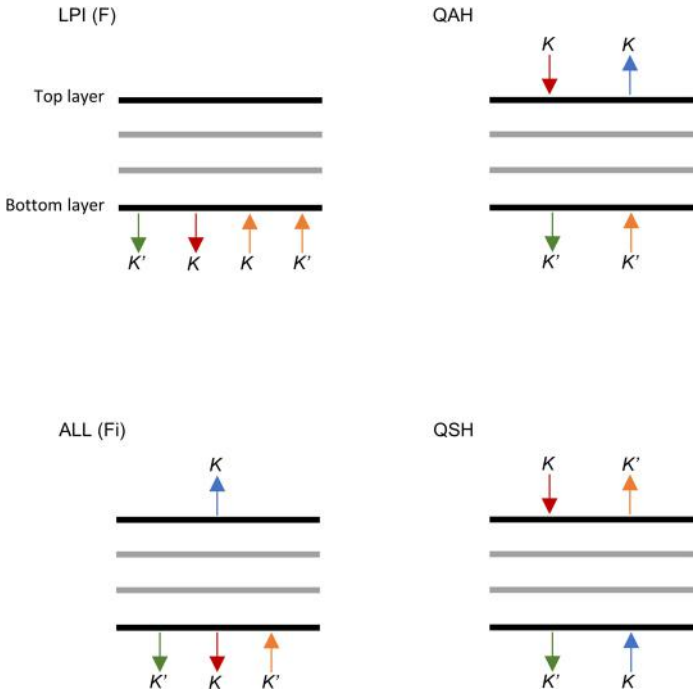

Extended Data Fig. 6 | Illustrations of spontaneous broken-symmetry states at charge neutral point. Illustrations of layer polarized insulator (LPI, also named as F phase), quantum anomalous Hall insulator (QAH), ALL (Fi) state and quantum spin Hall insulator (QSH). *K* and *K'* indicate two valleys, arrows indicate spin up and down, and black and grey planes indicate graphene layers.

https://doi.org/10.1038/s41565-023-01558-1

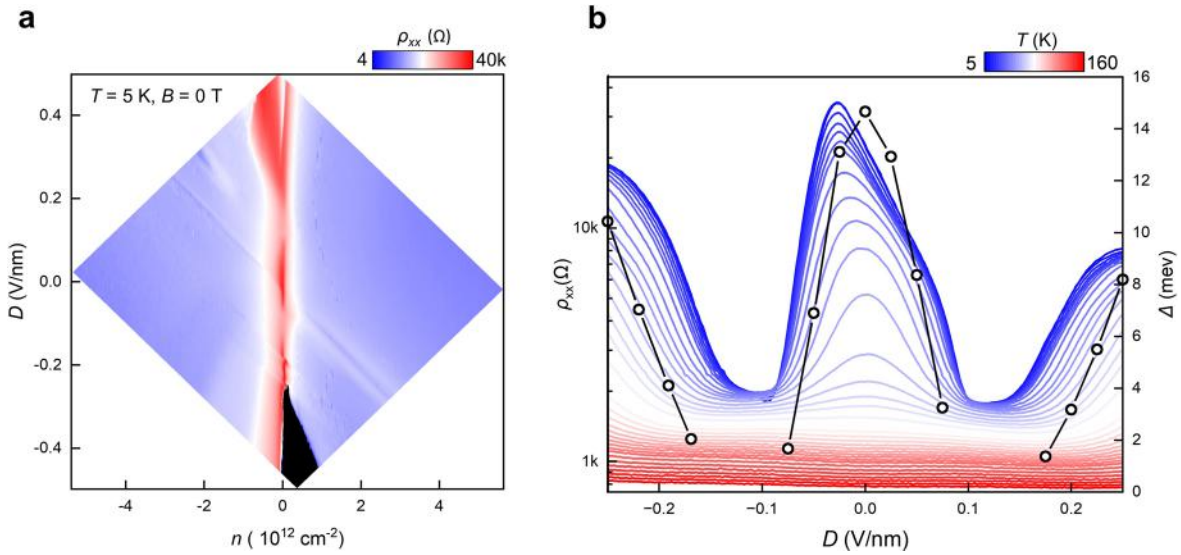

Extended Data Fig. 7 | Correlated insulating state at device 2. a, $\rho - n - D$ color plot of device 2, it shows a log color scale from 4 to 40 kΩ. **b**, Left axis corresponds to plot of ρ_{xx} at different D and fixed n and B of 0 for temperatures ranging from 1.5 K to 160 K. Right axis is the corresponding displacement field dependence of gap Δ. Device 2 gives almost the same gap with device 1 in the main text.

https://doi.org/10.1038/s41565-023-01558-1

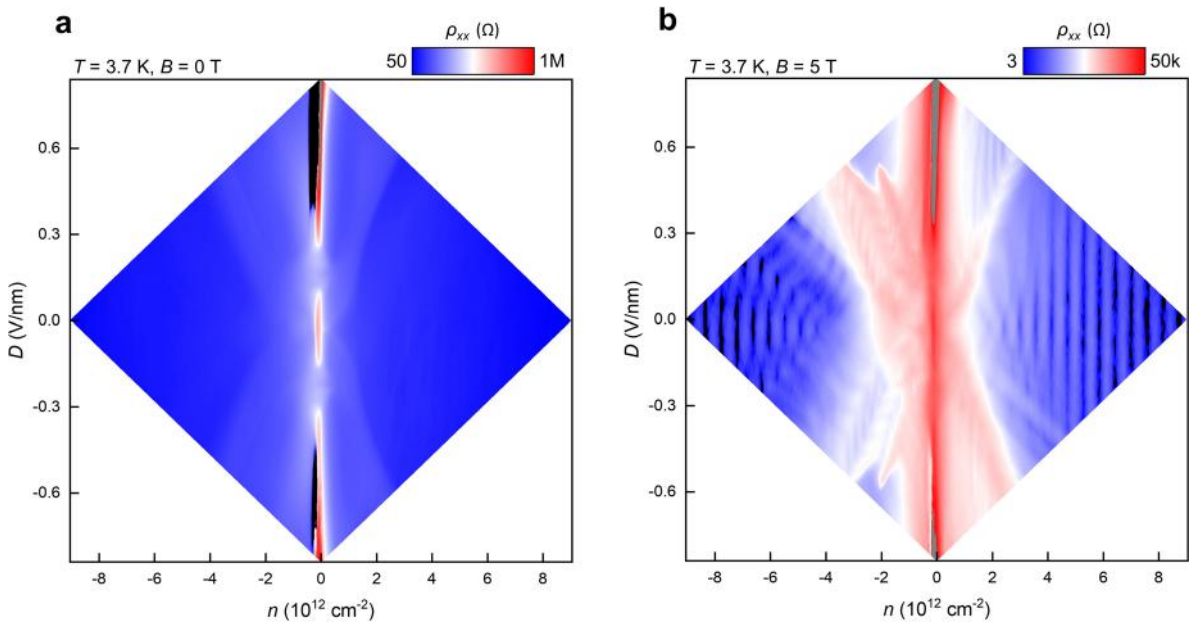

Extended Data Fig. 8 | Correlated insulating state and SP & SVP states at device 3. a, ρ - n - D color plot of device 3 when temperature T = 3.7 K, it shows a log color scale from 50 to 1 MΩ. **b**, Corresponding R - n - D color plot when B = 5 T. SP and SVP occur at the similar regions with device 1 in the main text.

https://doi.org/10.1038/s41565-023-01558-1

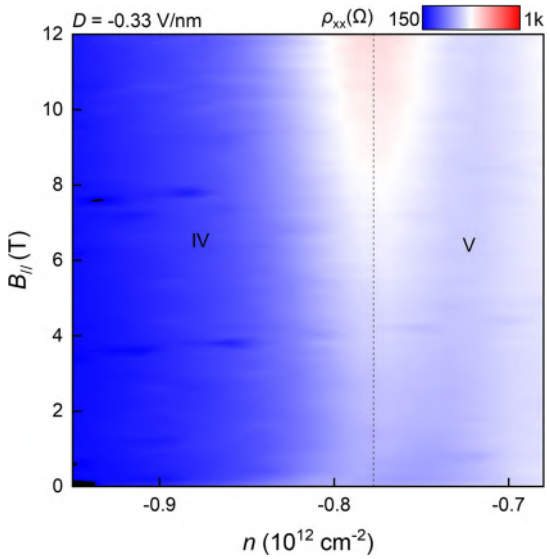

Extended Data Fig. 9 | Phase boundary between IV and V. $n - B_{//}$ color plot of resistivity at $D = -0.33$ V/nm between region IV and V. The phase boundary between IV and V doesn't move under in-plane magnetic field.

https://doi.org/10.1038/s41565-023-01558-1

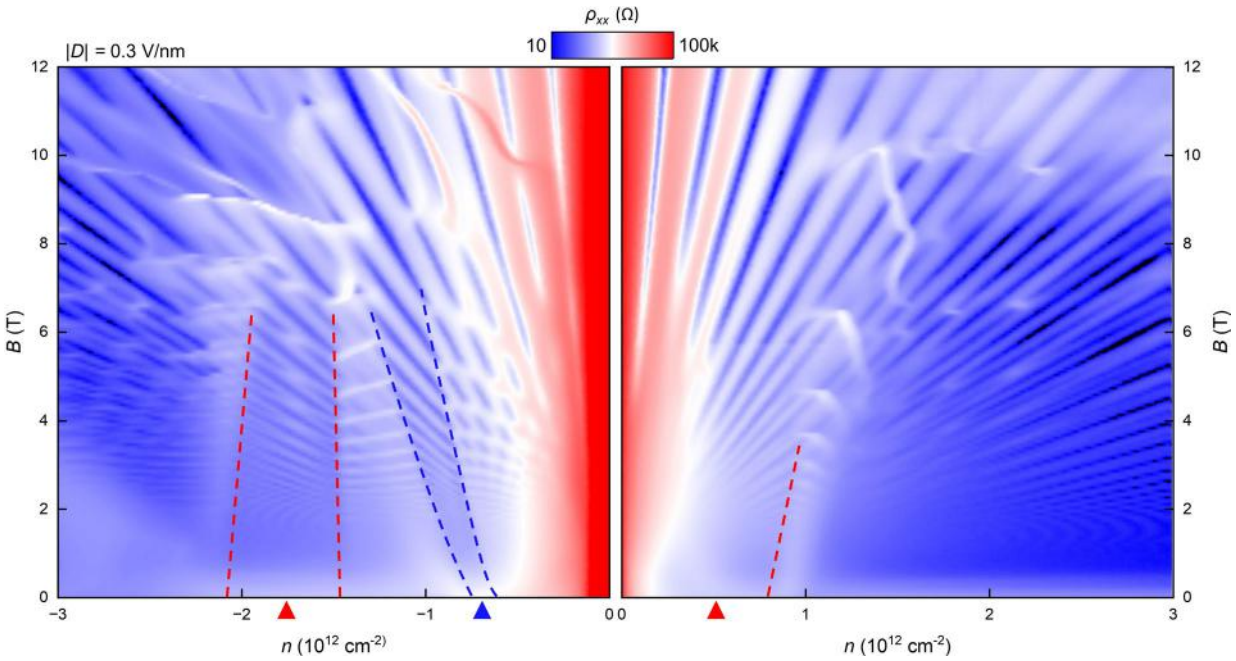

Extended Data Fig. 10 | Landau level fan of device 1 (the same sample in the main text). $\rho - n - B$ color plot of device 1 at $D = 0.3$ V/nm when $T = 1.5$ K. SP and SVP states are also prominent in the landau level fan diagram which is indicated by blue and red triangles, and their area would develop with magnetic field since the Zeeman energy of spin and orbital should be changed (red and blue dashed lines show the boundary of SP and SVP. above the dashed line, all the degeneracy is open by the large magnetic field). The area of the SP metal indicted by the left hand side red triangle is almost unchanged, we ascribe it as a fully spin polarized region but the SP metal indicted by the right hand side red triangle as a partially spin polarized region.